Computer Communications 190 (2022) 154–165

Contents lists available at ScienceDirect

Computer Communications

journal homepage: www.elsevier.com/locate/comcom

Autonomous flying IoT: A synergy of machine learning, digital elevation, and 3D structure change detection

Faris A. Almalki [a], Marios C. Angelides [b,*]

[a] Department of Computer Engineering, College of Computers and Information Technology, Taif University, Kingdom of Saudi Arabia
[b] Brunel Design School, College of Engineering, Design and Physical Sciences, Brunel University London, Uxbridge, United Kingdom

ARTICLE INFO

Keywords:
Internet of things
Unmanned aerial vehicles
Machine learning
Digital elevation model
3D structure change detection model
Aerial imaging
Remote sensing

ABSTRACT

The research work presented in this paper has been funded by a national research project whose aims are to enable an Unmanned Aerial Vehicle (UAV) to fly autonomously with the use of a Digital Elevation Model (DEM) of the target area and to detect terrain changes with the use of a 3D Structure Change Detection Model (3D SCDM). A Convolutional Neural Network (CNN) works with both models in training the UAV in autonomous flying and in detecting terrain changes. The usability of such an autonomous flying IoT is demonstrated through its deployment in the search for water resources in areas where a satellite would not normally be able to retrieve images, e.g., inside gorges, ravines, or caves. Our experiment results show that it can detect water flows by considering different surface shapes such as standing water polygons, watersheds, water channel incisions, and watershed delineations with a 99.6% level of accuracy.

1. Introduction

The application of Artificial Intelligent (AI) is one of the main drivers of the Fourth Industrial Revolution's (4IR) Internet of Things devices and unmanned Aerial Vehicles (UAVs) is fueling the revolution. Equipping a UAV with sensors and machine learning capabilities will turn the eye-in-the sky into an autonomous flying IoT with immediate benefits.

From a communications perspective, UAVs may act as an alternative to satellites, but without the distance penalty, launch and maintenance cost and complexities, and offering more flexibility, rapid deployment and portability, and Line of Sight (LoS) connectivity. From a remote sensing perspective, UAV may capture, for example, high resolution data rapidly, at low cost and risk and importantly whilst flying near the target area which may normally be inaccessible to satellites. From an IoT perspective, a UAV may be trained in autonomous flying and terrain change detection using a machine learning approach. Such an autonomous flying IoT, would be useful, for instance, for smart farming, terrain monitoring, emergency response, ecological research [1–4].

From a combined perspective, UAVs are now challenging the traditional view that aerial reconnaissance and photogrammetry is a job primarily for satellites. UAVs offer terrestrial close-range, in contrast to satellites' remote from space photogrammetry, access to areas that are normally inaccessible to satellites, and without the distance, launch and maintenance cost, and deployment time penalties of satellites [5,6]. Deploying a UAV to recognize terrain morphology requires the use of a DEM or Digital terrain model (DTM), or Digital surface model (DSM) [7,8]. Fig. 1 presents the landscape of geomatics techniques, sensors, and platforms in relation to scene size and complexity [5].

However, enabling a UAV to fly autonomously requires that the UAV is trained to recognize the morphology of the terrain it flies over, using the terrain's DEM. Furthermore, enabling a UAV to carry out continuous reconnaissance missions over the same terrain requires that the UAV is trained to detect terrain morphology changes with the use of a 3D SCDM. Such a flying IoT will be very useful for reconnaissance missions that rely on detecting terrain changes as the first signs, for example, of water resources, in areas that cannot sustain human life, and which are not normally accessible by a satellite to retrieve terrain imagery.

The aim of this paper is to present a machine learning framework that enables a Convolutional Neural Network (CNN) to train a UAV loaded with spectral cameras to fly autonomously over a terrain and detect terrain changes over several missions using a DEM and a 3D SCDM respectively. The paper demonstrates the usability of the resulting autonomous flying IoT during reconnaissance missions aimed at searching for water resources. This will also require the use of a specialist Water Detection Model (WDM) that will help the CNN train the UAV narrow its search to detecting water signs. Naturally the resulting framework can be applied to other areas where a model like WDM exists that will help the UAV narrow its search as it is the case with WDM.

The rest of this paper is organized as follows: Section 2 reviews related research; Section 3 presents the proposed autonomous flying

* Corresponding author.
E-mail addresses: m.faris@tu.edu.sa (F.A. Almalki), marios.angelides@brunel.ac.uk (M.C. Angelides).

https://doi.org/10.1016/j.comcom.2022.03.022
Received 18 December 2021; Received in revised form 26 March 2022; Accepted 29 March 2022
Available online 6 April 2022

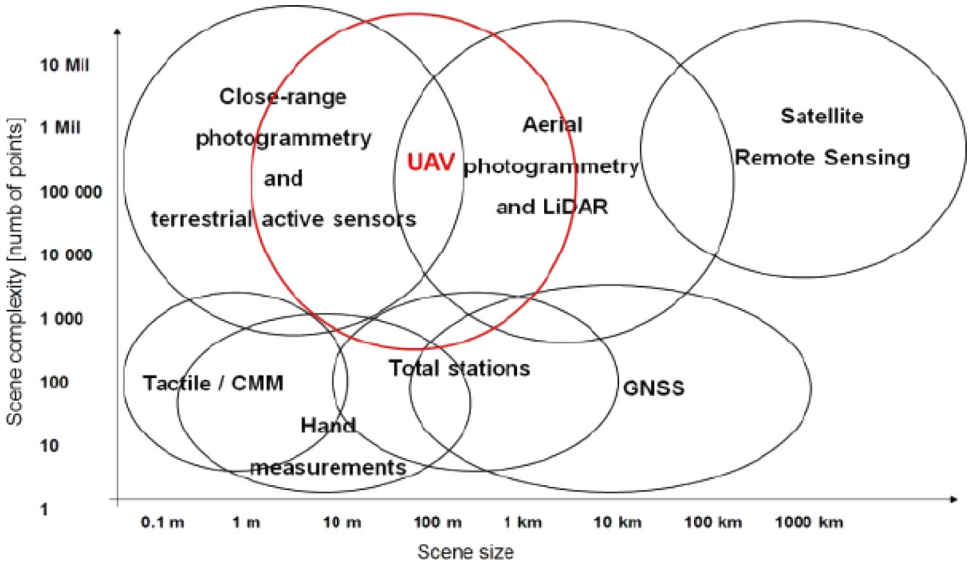

Fig. 1. UAV photogrammetry against other approaches.

IoT UAV along with the intelligent CNN framework that supports its reconnaissance operations; Section 4 presents simulation results; Section 5 concludes.

2. Related research

The search criteria for sourcing related research works to review include types of UAV platforms, low altitude missions, autonomous flying, types of aerial imaging, standalone topologies, change detection, and intelligent frameworks with preference for works that broadly fit our application area. The section concludes with a research windup table, followed by a presentation of the research gaps identified, and our own research motivations for prototyping the proposed autonomous flying IoT.

An aerial platform for Marine Ecosystem Restoration (MER) is presented in [9], which aims at monitoring water quality within a broad impacted area before and after restoration. Results infer that aerial imaging via UAV can deliver flexibility in temporal and spatial resolution, especially in enabling access to hard-to-reach zones with little to no disturbance.

The use of a DEM for terrain mapping, e.g., soil and water, is presented in [10]. This is achieved with remote sensing images in the loess plateau. Remote sensing may also be used for soil and water conservation for sustainable farming. The cost-effectiveness of using a UAV and DEM for spatial and temporal data resolution in hydrological modeling and water resource management is emphasized in [11].

The performance for flood estimation using experimental Fixed-Wing UAVs is evaluated in [12] by taking aerial imaging at an altitude of 325 m and using a DEM and Light Detection and Ranging (LiDAR). The results reveal that aerial imaging for flood assessment applications are reasonable within a 10.3 cm pixel size.

A study in Italy on the use of UAV and DEM for watershed detection from an altitude of 100 m is presented in [13]. Results yield high resolution and accuracy between 15 and 30 cm with low surveying cost and time in contrast to LiDAR. The results support small basin flood mapping.

A UAV aimed at recognizing objects using DSM aerial imaging at altitudes of 300 m and 500 m is simulated in [14]. The study covers an area of 0.51 km ^{2} in the center of University Technology Malaysia. The simulated results show the ability to recognize different land features including water bodies. When applying a structure from motion (SFM) approach, the photogrammetric processing accuracy rises to around 90%.

An aerial photogrammetry study for observing water surfaces in a small stream in Denmark using UAV and DEM is presented in [15]. The experiment was conducted at 30 m and 70 m above ground level and results show that the UAV–DEM can retrieve highly accurate water surface elevation (WSE) observations.

Monitoring river morphology and bank erosion in rural France using UAV and DEM to retrieve imagery is discussed in [16]. At around an altitude of 130 m, the spatial resolution of UAV images is of sufficient quality to survey small changes between 10 and 20 cm. The results suggest an ability to survey and monitor rivers efficiently, at a minimum cost, complexity, cloud cover and logistical problems in comparison to satellites.

Empirical evaluation of a photogrammetry streamflow model taken in rural Wisconsin using UAV and DTM is introduced in [17]. Taken from an altitude of 80 m, the hydrologic model structure serves as good case on how UAV data can be sourced at low-cost but serve equally decision making.

The UAV and DSM utility for monitoring marshes in rural Central California is evaluated in [18]. Working from an altitude of 30 m is found to be ideal for taking aerial images with high spatial variation of areas that are otherwise difficult to access on foot.

An experimental study that compares the performance of two UAV approaches over North Carolina is presented in [19]. The first approach aims at 3D Water Surface Reconstruction using structure from motion (SFM) and CNN whereas the second approach aims at 3D Water Reconstruction using DEM and CNN. The root mean squared error (RMSE) assessment tool was used to compute the floodwater depth error. The RMSEs were 0.34 m and 0.26 m respectively.

A fixed-wing UAV with DTM for analyzing the quality and accuracy of geomorphology photogrammetry that includes water bodies is proposed in [20]. The work highlights the need for optimization through several variables that would affect the performance of the aerial DTM survey, including UAV altitude and speed, orientation of the flight lines, image overlap, and camera configuration, e.g., shutter speed, frame rate, focal length. Results confirm that the RMSE performance indicator can deliver DTMs with high accuracy when the photogrammetry variables are optimized. It has been observed that as the UAV altitude increases from 70 m up to 150 m so does the RMSE which affects accuracy. The RMSE remains almost constant below 70 m.

A UAV with LiDAR and DEM that detects pipe-related depressions in rural Poland is presented in [21]. Using area topography, the study reports a rate of success between 76 and 80%. This drops down to a rate between 45 and 50% depending on the area morphology.

A UAV with a digital orthophoto map (DOM) photogrammetry for assessing landslide behavior in China is introduced in [22]. The deep learning image recognition technique of RetinaNet is utilized for feature extraction. Results show a notable influence on the distinguishability index for landslide cracks, and these are validated using a receiver operating characteristic (ROC) curve that reflects the relation between the true positive rate (TPR) and the false positive rate (FPR).

The study of a UAV building a DSM of hyperspectral data on ground characteristics including water signs from an altitude of 80 m above the ground in China is presented in [23]. The study considers different intelligent object classification schemes including a classification and regression tree (CART), and vegetation indices (VIs). The results indicate an overall accuracy of 88% and a kappa coefficient of 0.87 with aerial feature identification.

Remote sensing in hard-to-reach regions highlights the advantages of UAVs over satellites and access on foot. The use of UAV with a thermal camera for remote mapping of underground caves and rockslides from an altitude of 100 m is presented in [24]. The UAV's DSM data help with detection of water signs from images retrieved. A multifunctional UAV with thermal camera and Synthetic Aperture Radar (SAR) deployed during search and rescue operations of missing persons in complex environments is presented in [25]. Experimental results advocate improved connectivity between the UAV and ground control station through implementation efficiencies.

A UAV with DSM for geological spatial modeling of underground caves from an altitude of 170 m in Indonesia all in support of local tourist attractions such as caving, and body rafting is reported in [26]. Initial experimental results confirm the usability of the aerial imagery from such a high altitude. A UAV with a DTM that uses a multi-spectral camera from an altitude of 300 m for AGB estimation of tropical mountain forests including ravines is reported in [27]. The results showcase how effective UAVs can be in mapping narrow or inaccessible regions to fill in gaps in existing imagery.

A UAV that uses a DEM model and Structure from Motion (SfM) software to estimate the ice volume and thickness on riverbeds and riverbanks from an altitude range of 20 to 50 m above ground is proposed in [28]. The results obtained from 11 flight missions yield acceptable manual measurements. A UAV that uses a DEM model to collect spatial high-resolution data on coastal line vulnerability from an altitude of 40 m above ground is presented in [29]. The aim is assessment of short-term morphological and topographic changes on water bodies along coastal lines.

A UAV that uses an agrometeorological DSM for reducing water consumption and ensuring sustainability in agriculture is introduced in [30]. The UAV collects a wide range of spatial and thermal image data that showcase the efficiency of aerial imaging for irrigation management.

A UAV that uses a DEM to identify water erosion in open mining zones from an altitude of 115 m is proposed in [31]. The imagery the UAV collects autonomously helps with calculating the volume and speed of erosion and identifying watersheds. A UAV that uses a Neural Network with a DEM model for flood modeling in a dense urban environment from an altitude ranging to 100 m is presented in [32]. A study that makes use of a UAV with DEM, SfM, Multi-View Stereo (MVS), aerial photogrammetry and remote sensing to determine shallow waterbodies is presented in [33]. Initial results indicate high accuracy in depth measurements.

2.1. Research motivation and contribution

Table 1 summarizes the findings from our review of the literature in terms of issues being addressed and those gaps that remain the latter of which have motivated our own research work. The research review reveals several approaches in response to on-going challenges that still need addressing, thus, motivated by what related studies reveal, the proposed model not only aims to address on-going challenges, but also offers added value. The key difference between the proposed model against what is reported in the literature is, primarily, the combined use of:

- A DEM for autonomous flying over target area,
- A 3D SCDM for detection of terrain changes,
- CNNs for initiating autonomous flying and terrain change detection,

and, secondarily, testing the usability of such autonomous flying IoTs in addressing a life-critical problem that has recently become much more than just a pastime, i.e., searching for water resources using a WDM in those regions across the world where water resources are scarce.

3. Proposed work

The main advantage of loading a UAV with both a DEM and a 3D SCDM arises from the need to have an eye-in-the-sky but as near the ground as possible to detect terrain changes over time in those areas that are inaccessible by satellites for image retrieval, e.g., a gorge, a ravine, or inside caves. Therefore, the aim of this gain-of-function model is threefold: First, to enable a UAV to fly autonomously over a target terrain, second, to detect terrain surface changes in the target terrain and third, to detect, in our case, possible water flows as a proof of concept.

To achieve the first aim of enabling an autonomous flying UAV, we train a Reinforcement Learning (RL) Network with a DEM to establish both a precision aerial imagery and the flight-plan for the UAV over the target terrain. To achieve the second aim of detecting terrain surface changes, we train a deep learning CNN with a 3D SCDM to recognize such changes. In achieving the third and more specific aim of detecting changes because of possible water flows, we also train the deep learning CNN with a Water Detection Model (WDM) of water flow classifications, including standing water polygons, watersheds, water channel incisions, and watershed delineation. Regions of interest are areas void of people because of lack of water resources that will sustain human life.

3.1. The autonomous flying IoT framework

Fig. 2 shows a flowchart of the proposed autonomous flying IoT framework for water detection. The development of the projection matrices for DEM and WDM with which the NNs are initially trained are discrete events, whereas the development of the projection matrix for the 3D SCDM is a continuous event as this may evolve after each flight.

Fig. 3 offers a birds-eye-view of the entire framework architecture at the core of which is the CNN which is trained to fly autonomously using a DEM and to recognize change in the terrain surface, in our case for signs of water, using a 3D SCDM and a WDM. This is a notable shift from what has been previously reported in the literature and this is the novelty of this work, i.e., an autonomous flying IoT aiming at detecting water resources in remote areas in which the lack off cannot sustain human live and where neither satellites nor people can penetrate and retrieve imagery at ground level.

3.2. The autonomous flying IoT framework architecture components

This subsection discusses in detail each component of the autonomous flying IoT architecture.

Table 1
Related review wind up against the search criteria.

Authors	UAV type	Altitude (m)	Autonomous flying	Aerial imaging type	Standalone topology	Change detection	Intelligent framework
[10]	UAV	x	x	DEM	✓	✓	x
[12]	Fixed-wing UAV	325	x	DEM	✓	x	x
[13]	UAV	100	x	DEM	✓	x	x
[14]	UAV	300 - 500	x	DSM	✓	x	✓
[15]	UAV	30 - 70	x	DEM	✓	x	x
[16]	UAV	130	x	DEM	✓	✓	x
[17]	UAV	80	x	DTM	✓	x	x
[18]	UAV	30	x	DSM	✓	x	x
[19]	UAV	x	x	DEM	✓	x	✓
[20]	Fixed-wing UAV	70 - 150	x	DTM	✓	x	x
[21]	UAV	35 - 50	x	DEM	✓	x	✓
[23]	UAV	80	x	DSM	✓	x	✓
[24]	UAV	100	x	Thermal with DSM	✓	x	x
[25]	UAV	15	x	Thermal with SAR	✓	x	x
[26]	UAV	170	x	DSM	✓	x	x
[27]	UAV	300	x	DTM	✓	x	x
[28]	UAV	25 - 50	x	DEM	✓	x	x
[29]	UAV	40	x	DEM	✓	✓	x
[30]	Fixed-wing UAV	30	✓	DSM	✓	✓	x
[31]	UAV	115	✓	DEM	✓	x	x
[32]	UAV	100	x	DEM	✓	x	✓
[33]	UAV	50 - 100	x	DEM	✓	x	x
Proposed	UAV	**100**	✓	**DEM**	✓	✓	✓

x denotes presence; ✓denotes absence

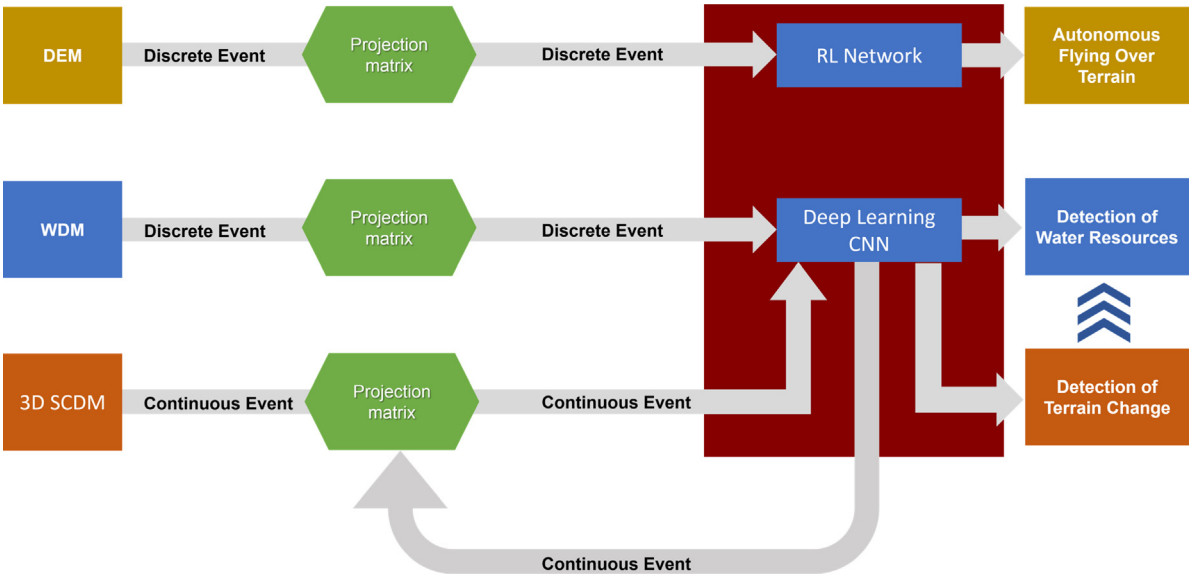

Fig. 2. Flowchart of the proposed autonomous flying IoT framework for water detection.

3.2.1. Component 1: The DEM of the target area

Fig. 4 shows two types of camera configurations, one for vertical and the other for oblique imagery which are necessary to achieve the precision and model texture quality whilst minimizing model deformity. Further, the combination between vertical and oblique aerial imagery would help with capturing images of overhanging watershed topography obscured by obstacles, e.g., treetop cover, overhanding rocks, blocking sunlight, water surface reflection, which may hinder the accurate planning and timing of a flight mission.

The initial DEM of the target area for input to the RL network will be based on previously known topography and this will be fine-tuned through aerial reconnaissance images and then pipelining these for structure processing which includes feature tracking, triangulation, and bundle adjustment, followed by positioning information, and dense matching of 3D point cloud analysis, and concluding with a validation. Pipelining is vital in estimating a projection matrix for images taken, feature detectors, enhancing the ground structure spatial resolution, eliminating noisy data, and interpolating the dense point cloud by using a mesh-grid generator. The DEM detail and precision has a direct effect on flight planning. Fig. 5 illustrates part of the principal method for fine-tuning the initial DEM. The development of the DEM is a discrete event from the point of view of enabling autonomous flying as once fine-tuned from the initial topography, the DEM will not change over time unless a significant major event has taken place, such as an earthquake or landslide, that may result in a change of topography [34,35].

The DEM is represented as Eqs. (1) and (2).

$$dh \approx dx\frac{h}{b} \tag{1}$$

$$h = Z_{01} - Z_{DEM} \tag{2}$$

where dh denotes height errors used as corrections, dx denotes parallax between two images, h denotes point height in DEM, Z_{01} denotes elevation of left image projection center, Z_{DEM} denotes elevation of DEM point, b denotes photo base.

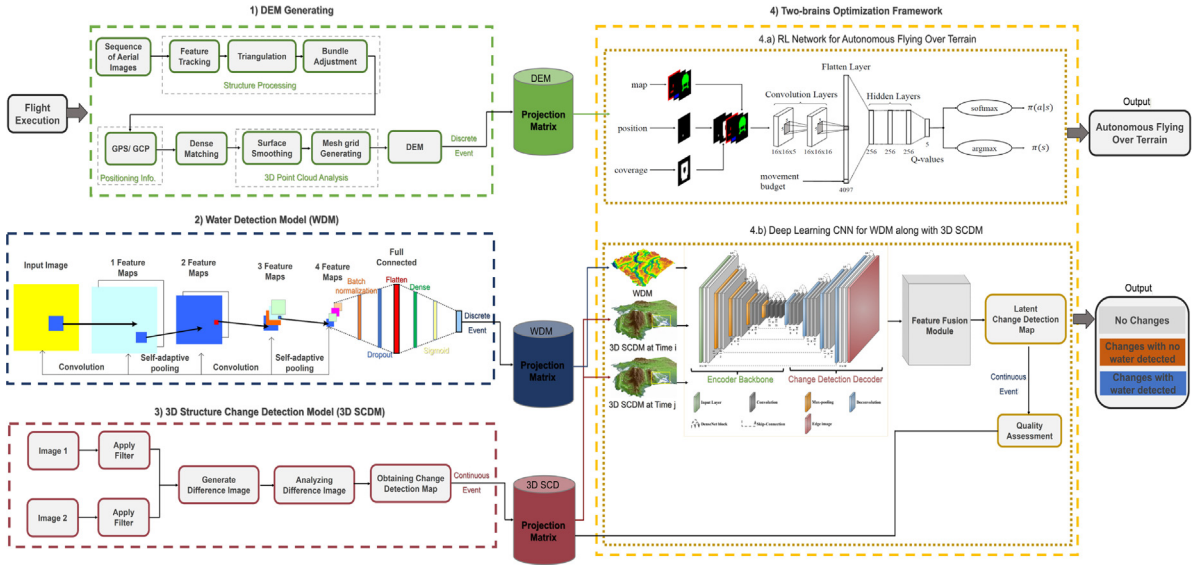

Fig. 3. The autonomous flying IoT framework architecture.

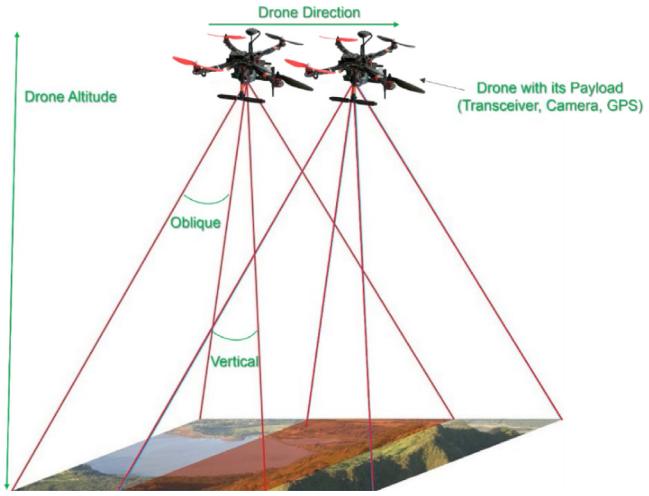

Fig. 4. UAV camera vertical and oblique configurations.

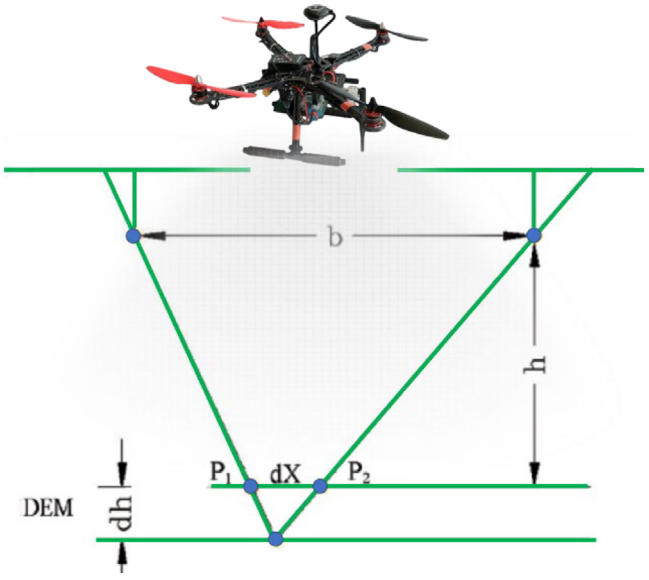

Fig. 5. Fine-tuning of a DEM.

3.2.2. Component 2: A WDM representative of the target terrain morphology

A WDM with detailed classifications of spectral and spatial data which are representative of the target terrain morphology is used to train the Deep learning CNN to detect signs of water flows, standing water polygons, watersheds, water channel incisions, and watershed delineations. The architecture of the NN consists of several connected layers such as convolution, pooling and fully connected. To achieve gain-of-function, additional layers of batch normalization, dropout and flatten, and a dense layer with sigmoid activation have also been included in this model to give the NN its learning trait. The batch normalization and dropout layers are used to improve normalization, rescaling, and shifting off the offset of input values, as well as to prevent overfitting in the model. The flatten layer converts the entire pooled feature map matrix into one-dimensional array which is then input to the dense layer.

The logistic sigmoid regression is used since this is a binary classification problem of identifying natural water channel incisions. The fully connected NN constructs feature maps through convolutional filters that can learn to identify high-level features from image properties and then predict the nature of each image pixel. The development of WDM is also a discrete event from the point of view of detection of water signs as the classifications of water signs that comprise the model will not normally evolve unless new classifications come to surface [36]. The WDM is represented as Eqs. (3) to (7).

$$X' = \frac{(X/\max) - \mu}{\sigma} \tag{3}$$

where X' denotes normalized data, max denotes maximum pixel value in the image, μ and σ denote mean and standard deviation of $X/\max$, respectively. The normalization is vital since aerial imaging have integer values, and initial weights are randomly selected between 0 and 1, thus, normalization to pixel values of the orthophotos prevents abnormal gradients.

The proposed deep learning CNN is trained with a backpropagation algorithm and stochastic gradient descent (SGD). This utilizes a mini-batch's backpropagation error to approximate the error of all training samples, which accelerate each cycle's weight update through a smaller back propagation error which speeds up the model convergence. The optimization is run to reduce the loss function (J) as Eq. (4).

$$J\left(X', W, b, \theta\right) = -\frac{1}{N}\left[\sum_{i=1}^{N}\sum_{j=1}^{K} 1\left\{y^i = t\right\} y_t^i\right] \tag{4}$$

$$y_t^i = \frac{\exp(\theta_t^T c)}{\sum_{j=1}^{K} \exp(\theta_t^T c)} \tag{5}$$

$$W_{t+1} = W_t - \lambda V_t - \alpha \nabla W \tag{6}$$

$$b_{t+1} = b_t - \lambda U_t - \alpha \nabla b \tag{7}$$

where W and b are parameters of the NN, θ is a parameter for the Sigmoid classifier, N denotes the number of samples, K denotes the number of land cover classes, $y^i = (y^i{}_1, \ldots . y^i{}_k)$ is the prediction vector geo by the Sigmoid classifier, y_t^i denotes the possibility of the ith sample label being t and is represented by (5).

Through backpropagation, (6) and (7) are adapted to update W and b in every layer, where λ denotes the momentum which help accelerate SGD by adding a fraction of the update value of the previous time step to the recent updated value, α denotes learning rate, ∇W and ∇b are the gradients of J, and t denotes the number of epochs during SGD.

3.2.3. Component 3: The 3D SCDM of the target area

A 3D SCDM may evolve continuously over the course of several search flights until either a water resource has been detected or the search is called off. Therefore, the development of this model is a continuous event from the point of view of detection of a terrain change as the model may evolve after every search cycle if a terrain change has been detected. Achieving detection accuracy requires an unsupervised CNN which has the ability of feature learning and uses a latent change detection map. This allows the network to learn of features from the input data and regularization parameters. When a change is detected in the target area the 3D SCDM is updated to help with future search missions [37]. The modeling of imagery at two different times i and j where $i < j$ is given as Eqs. (8) and (9).

$$\mathrm{SCDM}_i(x,y) = \underset{x',y'}{min} \left(\left(D_1(x,y) - D_2\left(x',y'\right) \right) \geq 0 \right) \tag{8}$$

$$\mathrm{SCDM}_j(x,y) = \underset{x',y'}{max} \left(\left(D_1(x,y) - D_2\left(x',y'\right) \right) \leq 0 \right) \tag{9}$$

where D_1 and D_2 are images, $x' \in [x-w, x+w]$, $y' \in [x-w, x+w]$ and (w) is window around a set of pixels.

3.2.4. Component 4a: RL network for autonomous flying IoT over terrain

The network uses a Double Deep Q-Network (DDQN), a type of Q-Learning with a cycle of interactions between an agent and its environment at each state. DDQN uses a Markov Decision Process (MDP) to plan a path. The MDP is described by the tuple (S, A, R, P), where S is a set of possible states, A is a set of possible actions, R is the reward function, and P is a deterministic state transition function [30]. In an N×N grid, the state space S is defined as:

$S = Map \times Coverage \times Position \times Movement\ Budget \times Safety\ Flag$

and represented as Eq. (10).

$$S = \mathbb{B}^{N \times N \times 3} \times \mathbb{B}^{N \times N} \times \mathbb{R}^2 \times \mathbb{N} \times \mathbb{B} \tag{10}$$

where $\mathbb{B}$ denotes the Boolean domain $\{0, 1\}$. The action space A contains five actions (North; East; South; West; Land). The state transition function is defined as: $P : S \times A \rightarrow S$. The reward function which is defined as: $R : S \times A \rightarrow \mathbb{R}$ maps the current state $s \in S$ and current action $a \in A$ to a real-valued reward and consists of four components:

- r_{cov} (positive) coverage reward for each target point that is covered by the UAV for the first time
- r_{sc} (negative) safety penalty in case the safety controller (SC) rejects the agent's proposed action
- r_{mov} (negative) constant movement penalty applied for every unit of the movement budget used
- r_{crash} (negative) penalty in case the UAV runs out of movement budget without having safely landed in a landing zone.

Q-learning updates iteratively the present state of the Q-function. When the optimum Q-function is identified, it constructs an optimum strategy by taking actions that maximize the Q-function. The target value is given as Eq. (11), while the corresponding loss function is given as Eq. (12).

$$Y^{DDQN}\left(s,a,s'\right) = r(s,a) + \gamma Q_{\theta'}(s', argmax Q_\theta(s',a')) \tag{11}$$

$$L^{DDQN}(\theta) = \mathbb{E}_{s,a,s' \sim D}(Q_\theta(s,a) - Y^{DDQN}\left(s,a,s'\right))^2 \tag{12}$$

where $\left(s,a,r,s'\right)$ stores experience tuples that have been collected by the agent during each interaction with the environment, θ refers to the number of trainable parameters, θ' refers to the parameters of the target network which can be updated as a periodic hard copy of θ or as a soft update $\theta' \leftarrow (1-\Gamma)\theta' + \Gamma\theta$. The back-propagating gradient is stopped at $Y^{DDQN}\left(s,a,s'\right)$. γ refers to the discount factor for the target value, and Γ refers to the target network update factor [38].

All DDQN layers are zero-padded for all channels, except for the first layer's no-fly zone channel which is reserved for the no-fly zone surrounding the mission grid. The rectified linear unit (ReLU) is the activation function for the convolutional layers, whilst the last layer is flattened and concatenated with the movement budget input. Fully connected layers with the ReLU activation are attached to this flattened layer. Choosing the argmax of the Q-values through a greedy policy is given as Eq. (13), which reflects the agent's learning progress

$$\pi(s) = \underset{a \in A}{argmax} Q_\theta(s,a) \tag{13}$$

During training, the sampled softmax policy for exploration of the state and action space is given as Eq. (14).

$$\pi\left(a_i | ss\right) = \frac{e^{Q_\theta(s,a_i)/\beta}}{\sum \forall a_j \in A e^{Q_\theta(s,a_i)/\beta}} \tag{14}$$

where β refers to a temperature parameter.

Training the RL network commences with resetting the state, choosing a random UAV starting position and a random movement budget. Training continues if the movement budget is greater than zero and the UAV has not landed and finishes either when the UAV lands or the movement budget decreases to zero. Then, another round of training starts unless the maximum number of training rounds N_{max} has been met.

3.2.5. Component 4b: Deep learning CNN for terrain change and water resources detection

The Deep Learning CNN uses both the WDM and the evolving 3D SCDM for feature extraction and classification therefore a 3D fully connected unsupervised CNN is needed, one that makes use of a latent change detection map and comprise of three modules: feature learning, a single-stream feature fusion, and unsupervised noise modeling. This is represented as Eqs. (15) through to (20) [39–41]. Convolution is a basic feature learning component represented as Eq. (15).

$$y_{ij} = f_1(\left\{ x_{si} + \delta_{i,S_j} + \delta_j \right\}, 0 \leq \delta_j, \delta_j \leq k) \tag{15}$$

where y_{ij} denotes the convolution output, which is also used as input to the next layer, f_1 denotes a specific operation for the input layer, x_{si} denotes input data, i, j denote a spatial coordinate, s denotes the convolution stride, and k denotes the kernel size. When loading the convolution layers, high semantic-level features are extracted, whereby if s is set to 2 then the spatial size of the output will be half of the input size at the convolution layer. However, since deconvolution is a transposed convolution type which is used to enlarge the output spatial size, the output spatial size will be twice the size of input.

A fully connected convolution network detects a terrain change by extracting the deep features of a target terrain at different times and this is represented as Eqs. (16) and (17).

$$F_{SCDMi} = f_{decoder}\left(f_{encoder}(SCDi)\right), \quad F_{SCDMi} \in \mathbb{R}^{\{N,C,H,W\}} \tag{16}$$

$$F_{SCDMj} = f_{decoder}\left(f_{encoder}(SCDj)\right), \quad F_{SCDMj} \in \mathbb{R}^{\{N,C,H,W\}} \tag{17}$$

where $SCDMi$ and $SCDMj$ are the terrain structure changes detected from search mission i to j respectively, $f_{decoder}$ denotes decoder, $f_{encoder}$ denotes encoder, $F_{SCDMi} \in \mathbb{R}^{\{N,C,H,W\}}$ and $F_{SCDMj} \in \mathbb{R}^{\{N,C,H,W\}}$

denote the final convolution feature maps which will be used to update the SCDM with the changes detected and N, C, H, W denote batch size, channel size, height, and width of the final feature maps, respectively.

Detecting a change is established when a significant number of pixels change from mission i to j with reference to the classifications included in WDM. A feature-level fusion is applied to update the SCDM. Generating a change detection map is represented as Eqs. (18) to (20).

$$F_{i,j} = concat(F_{SCDMi}, F_{SCDMj}) \tag{18}$$

$$F_{i,j} = \frac{1}{2} F_{SCDMi} + \frac{1}{2} F_{SCDMj} \tag{19}$$

$$F_{i,j} = F_{SCDMi} - F_{SCDMj} \tag{20}$$

where F_{SCDMi} and F_{SCDMj} represent the final feature maps at the highest spatial resolution and abstract level, $F_{i,j}$ in (11) uses concatenation to fuse multiple features, $F_{i,j}$ in (19) uses element-wise summation to fuse two feature maps, $F_{i,j}$ in (20) uses element-wise subtraction for feature fusion. Once these feature fusion functions conclude, the feature maps obtained are used in the following noise module to update the change detection map.

The change detection in the 3D SCDM does not includes ground truth labels since we use an unsupervised change detection method to train the fully connected convolution network. The training dataset Y_p is represented as Eq. (21).

$$Y_p = \{y_i \in \mathbb{R}^{(H,W)}, i = 1, \ldots\ldots, k\} \tag{21}$$

The network learns the latent change detection map, following which should be trained to generate the actual change detection map with the training dataset Y_p and k which denotes existing change detection maps. Therefore, the noise module is represented as Eqs. (22) to (24).

$$y_i = f\,(SCDMi, SCDMj, \Theta) + n_i \tag{22}$$

$$n_i = y_i - \overline{y}_i \tag{23}$$

$$\overline{y}_i \in^{(H,W)} = f_d(F_{SCDMi}) \tag{24}$$

where f denotes the whole network, Θ denotes convolution network parameter, n_i denotes noise map which is subject to a zero-mean Gaussian distribution, $\overline{y}_i$ denotes estimated change map, $\overline{y}_i \in^{(H,W)}$ denotes the actual change detection map, and f_d denotes the decoder network.

To enforce the computed noise map to follow the prior Gaussian distribution, Kullback–Leibler (KL) divergence loss is used. Hence, the loss function is represented as Eq. (25).

$$L_{KL}(\Theta, \sum) = KL(p(\sum) \parallel q(\widehat{\sum})) \tag{25}$$

where $p(\sum)$ denotes the corresponding distribution, and $q(\widehat{\sum})$ denotes the prior Gaussian distribution. This formula is vital since the noise is separating the training dataset from change detection. Performance is improved in an unsupervised manner.

3.2.6. Component 5: Projection matrices

The flowchart on Fig. 6 below depicts the part of the process involving the three projection matrices. This commences with generating a DEM for the first brain to train the UAV to fly autonomously over a target terrain without human intervention. A WDM is generated from existing imagery on water polygons, watersheds, water channel incisions, and watershed delineations for the second brain to train the autonomous UAV to detect signs of water resources over the target terrain with reference to this model.

A 3D SCDM is continuously updated with terrain surface imagery for the second brain to train the autonomous UAV in detecting terrain surface changes across flights that may now suggest the presence of water resources with reference to the WDM. After each flight there are three possible outcomes: no changes, terrain change but no water resources detected, terrain changes and water resources detected. Image resolution, the altitude, latitude, and longitude of images taken by the UAV, flying time of the UAV, wind speed and direction are the core data set that populates the projection matrices. The cycle continues until either a maximum number of flights or water resources have been detected.

Table 2
RL network parameter settings.

Parameter	Value
No. of Images	1000
Steps	50
Batch size	30
Learning rate	0.0001
Camera linear velocity	2 m/s
Training iteration	6000
Discount factor	0.99
Target factor	0.01
Exploration Constant	0.9
Action time interval	0.4 s
UAV Altitude	10-40 m
Path average distance	3 km
Path average width	47 m

4. Simulation

Pre-flight UAV, and camera settings are input to a Mission Planner tool before the first mission flight. Developing a UAV flight-plan includes take-off and landing sites, altitude, speed, flight mode, path-plan which are all necessary for aerial imaging and watershed detection. Fig. 7 demonstrates the Mission Planner tool calibrated with these parameters including search methods such as: Strip, Line, and Grid. Stripe and Grid use double-line search which is effective but time consuming. Thus, we use line search which is efficient for outdoors. In the search for water resources over the Snake gorge and ravine in the Arabian Peninsula, we use Google Maps for aerial imaging, as Fig. 8 shows footage over and inside the Snake gorge.

4.1. Training the two-brains

The first brain relates to the RL network supporting autonomous flying over the terrain. Training the RL network commences with resetting the state, choosing a random UAV starting position and a random movement budget. It continues if the movement budget is greater than zero and the UAV has not landed and finishes either when the UAV lands or the movement budget decreases to zero. Then another round of training commences unless the maximum number of training rounds N_{max} has been met. Table 2 shows the parameter settings for the RL network. Fig. 9 shows a sample of a DEM image taken from inside the Snake gorge by the UAV. Deciding on the simulation parameters set broadly follows the examples in [40,41] and on the number of iterations is based on past practical experimentation and experience, and with the steps representing approximately 1% of the total number.

Fig. 10 shows the training results with 6000 iterations and accumulated rewards. Training ends when simulation reaches 6000 iterations, each of which is 50 steps. At the end of each iteration, the UAV resets to its initial state and receives observation feedback. In each iteration, the UAV seeks to make the highest number of steps to achieve a high reward point. Light blue denotes the actual reward value for the iteration, whilst dark blue denotes the mean rewards after 50 steps. All learning, decision making and action taking during each step is pitched against a level of reward on the way to a maximum reward level.

Fig. 10 shows that at the start of training, when the UAV is beginning to establish its correct flying behavior, rewards are below zero. The lowest reward on the line chart denotes a UAV crash, which is an expected outcome during training. Arbitrary or incorrect flying behavior decreases over time and reward values are gradually increasing towards positive rewards. Training iterations stop when the UAV either meets its training goals, or its level of reward values become

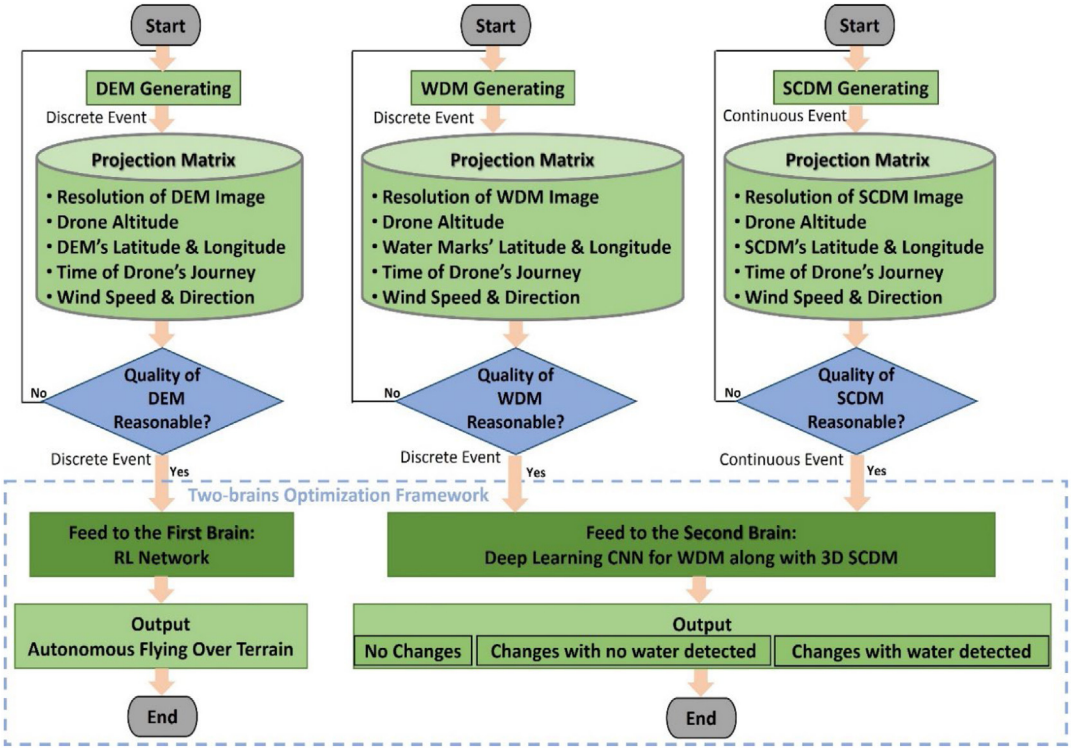

Fig. 6. Projection matrices.

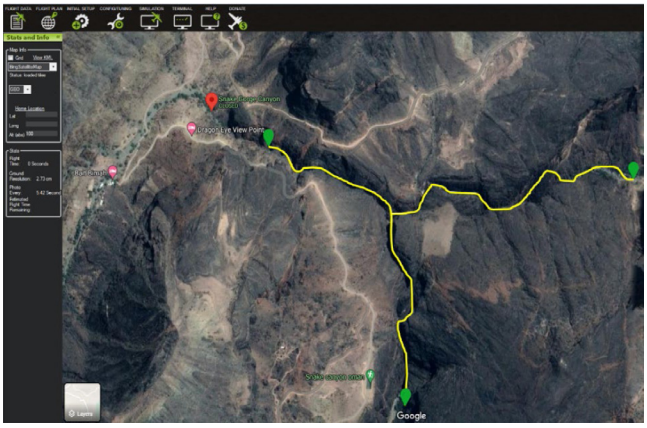

Fig. 7. The mission planner tool calibrated.

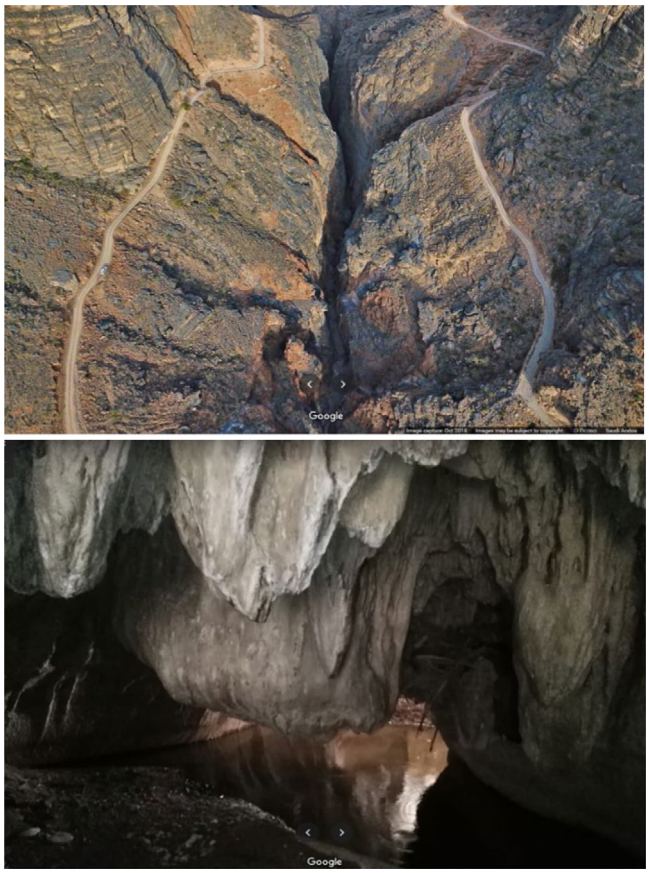

Fig. 8. Footages of over and inside the Snake gorge.

stable, or the number of iterations reach the set maximum. UAV crash episodes occur regularly over the first 1487 steps but, thereafter, the UAV corrects its flying behavior over the training environment, and no further crash episodes occur over the next 2500 steps. At approximately step 4000, the UAV has its first crash episode as it learns to avoid obstacles in its flight path, but, thereafter, the mean reward values increase as the UAV has learned to fly autonomously and avoid crashing on obstacles along its flight path. Noticeably, before reaching the end of training, the UAV does not crash with any obstacles along its flight path until during its last iteration cycle of 6000.

The second brain is used to train the autonomous UAV to detect changes over the terrain with reference to the 3DSCDM and then determine if any of these are new signs of water resources since the last reconnaissance mission with reference to the WDM. Fig. 11 shows a reconnaissance image taken inside the Snake gorge where in the green square a water sign is detected with reference to the WDM, but none are detected in the red square. The CNN can expect to detect water signs, but errors are also expected to occur. Superpixel segmentation

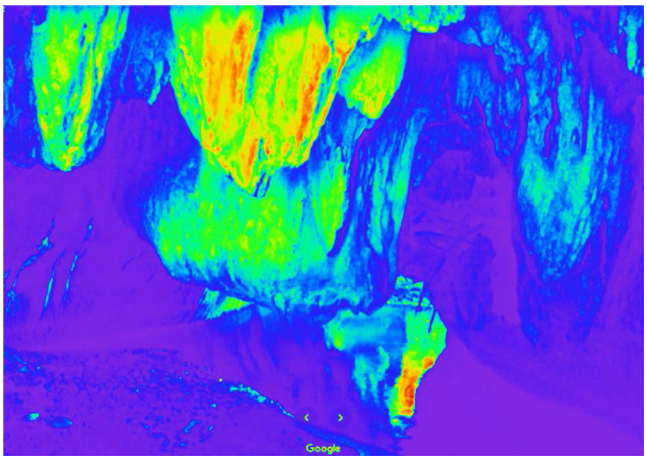

Fig. 9. Sample of a DEM image from inside the Snake gorge.

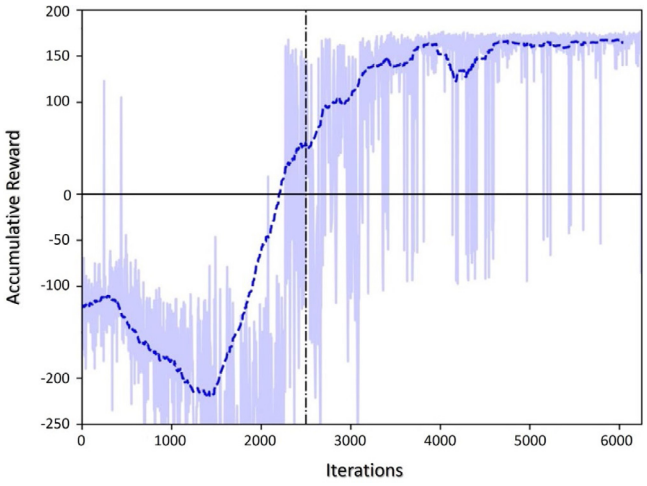

Fig. 10. Training results for autonomous flying over the terrain.

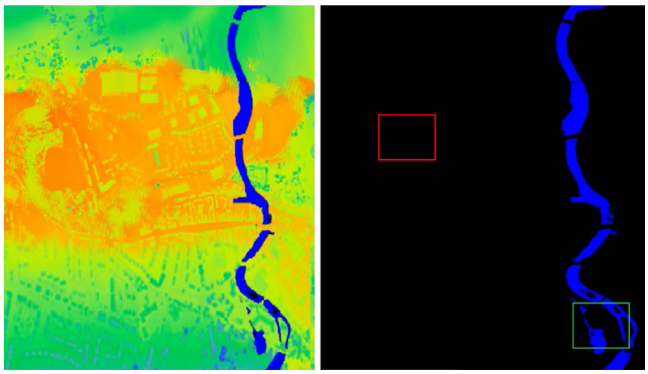

Fig. 11. Images of water signs inside the Snake gorge.

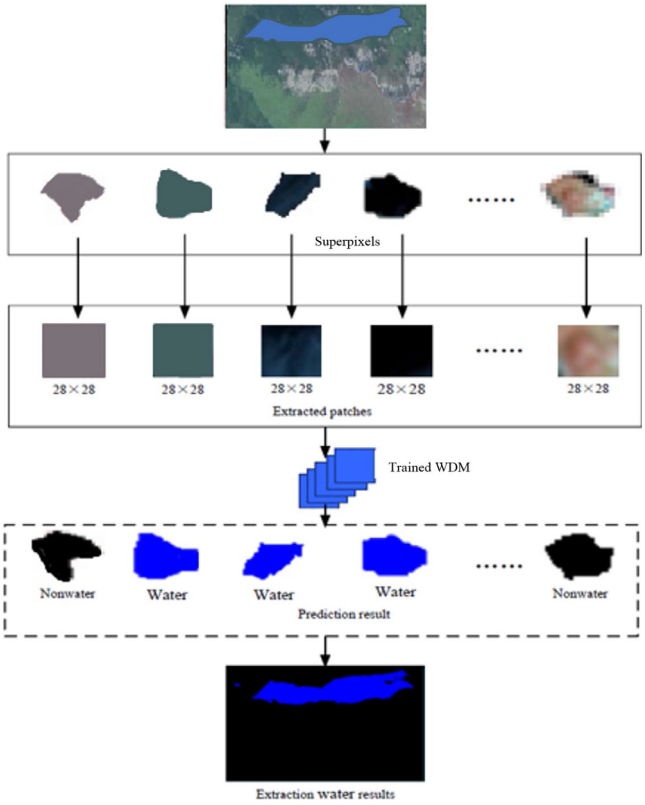

Fig. 12. Matching aerial images to water signs in WDM.

takes place to resolve by considering adjacent image blocks with alike color and brightness features as Fig. 12 shows.

The WDM dataset has been sourced from "Kaggle". This includes 500 images of water bodies taken from the sky for training and 500 images for testing and validation [42]. Fig. 13 shows the line chart for training and validation accuracy and loss with the use of WDM with both charts in sync. Training and validation accuracy tracks the performance of the classifier during training with the dataset and validation accuracy of the results. Training and validation loss tracks fitting of the model with the dataset, and validation loss indicates fitting of the model with new data. These two are key performance indicators in our proposed framework.

Fig. 13 shows an increase in accuracy and a decrease in loss over time which highlights the usefulness of the WDM in classifying image pixels into different class labels. The accuracy chart line indicates that the model can classify nearly all classes with relatively high level of accuracy. Training and validation accuracy is in synchronization with training and validation loss with a value near 0.94. It is significant that no overfitting has accrued from utilizing a dropout layer to prevent this from arising. The dropout layer deactivates neurons during training to reduce dependency on the training set and hence prevent the network from maintaining a memory of the dataset.

Fig. 14 showcases training with reference to the 3D SCDM: (a) reveals no changes, and (b) reveals some changes when comparing images taken of the same location but at different times. Using both the 3D SCDM and WDM, the second brain trains in feature extraction and classification to detect changes that may have occurred since the last reconnaissance mission with reference to the former and determine if these changes are water-related with reference to the latter. The deep learning CNN that uses the 3D SCDM is a fully connected unsupervised CNN that relies on a latent change detection map to specify whether there are changes or not.

Fig. 15 plots loss against iterations during training with the image dataset. During an iteration, the loss function calculates the loss on a subset of the entire dataset. The loss is formulated as the squared difference between the output of the model and the ground truth, and it is inversely proportional to the model robustness. The loss function is regularly applied during training to find the best parameter values for the overall model, e.g., weights. Due to the size of the dataset and the change detection function, the loss function requires between 7000 to 8000 iterations to converge. After 3500 iterations, the lose value shows a gradual decline in comparison to the period before that

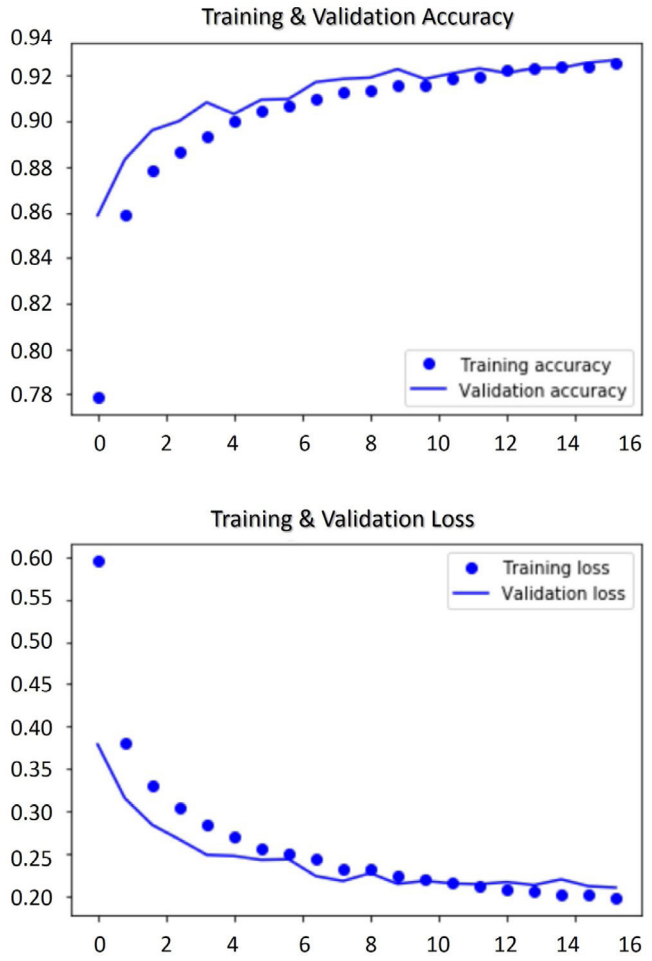

Fig. 13. Training and validation with the WDM.

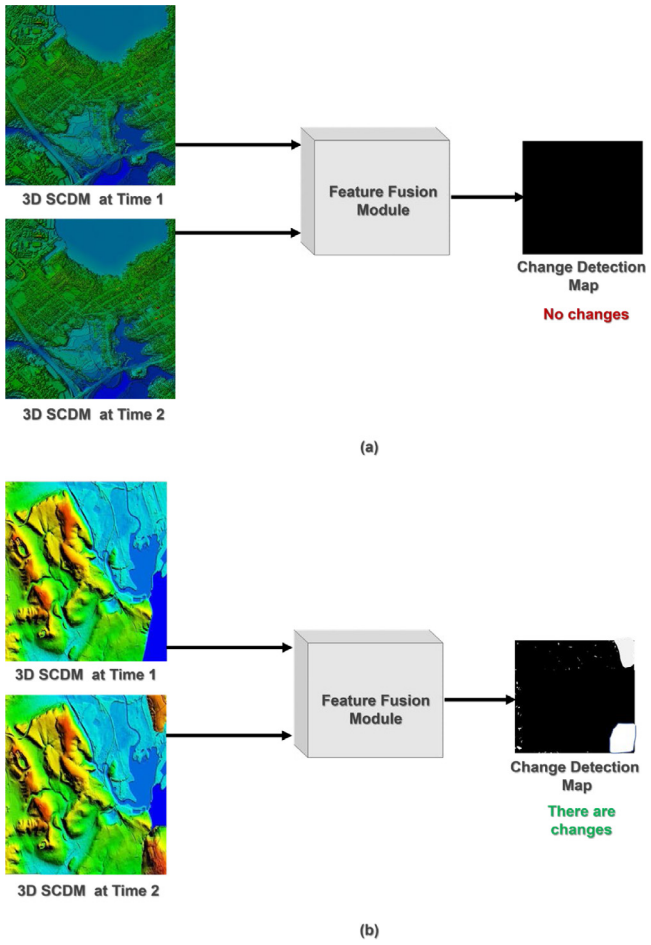

Fig. 14. Training with the 3D SCDM.

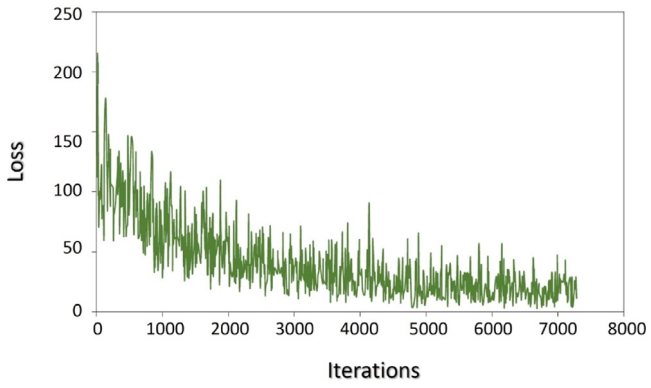

Fig. 15. Training loss with the 3D SCDM.

where it clearly shows a steep decline. Overall, the line chart of the loss indicates that the training results are congruent with the training dataset accuracy.

4.2. Validation of the autonomous flying IoT framework

We deploy Overall Accuracy (OA) and Kappa Coefficient to evaluate success with change detection. The Kappa Coefficient is used as a consistency test for to the accuracy of classification whereas OA is used as a consistency test to the accuracy of classification. Kappa indicates the level of consistency between the change detection and the ground-truth map, with the kappa coefficient directly proportional to the performance of the corresponding method. OA and the Kappa Coefficient are represented as Eqs. (26) to (28).

$$OA = \frac{TP + TN}{TP + TN + FP + FN} \tag{26}$$

$$Kappa = \frac{OA - P}{1 - P} \tag{27}$$

$$P = \frac{(TP + FP)(TP + FN)}{(TP + TN + FB + FN)^2} + \frac{(FN + TN)(FP + TN)}{(TP + TN + FP + FN)^2} \tag{28}$$

where True Positives (TP) and True Negatives (TN) refer to the number of changed and unchanged pixels accurately detected respectively, and False Positives (FP) and False Negatives (FN) refer to the number of unchanged and changed pixels falsely detected as changed and unchanged respectively.

Fig. 16 shows an aerial DEM over the Snake gorge in the Arabian Peninsula, where the UAV acts as an eye near the ground in those narrow or covered areas where a satellite would not normally be able to retrieve images. With the focus of this work being the detection of water bodies inside narrow areas like gorges or caves using an intelligent framework onboard a UAV, a normalized confusion matrix is presented in Fig. 17 which is obtained from the two-brains optimization framework.

The confusion matrix of Fig. 17 shows the accuracy level of the proposed 3DSCDM and WDM. Rows depict the ground-truth and columns depict predictions. The confusion matrix reveals that a UAV on a remote sensing mission and flying at a low altitude can distinguish between water bodies and other features with a high level of accuracy. The maximum accuracy for the water body class comes very close to 1.0,

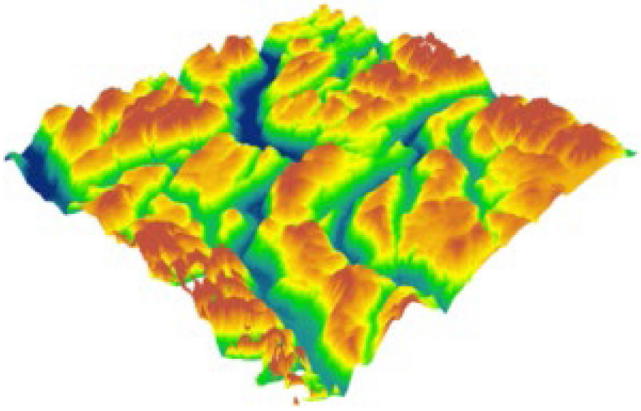

Fig. 16. Aerial DEM over the Snake gorge.

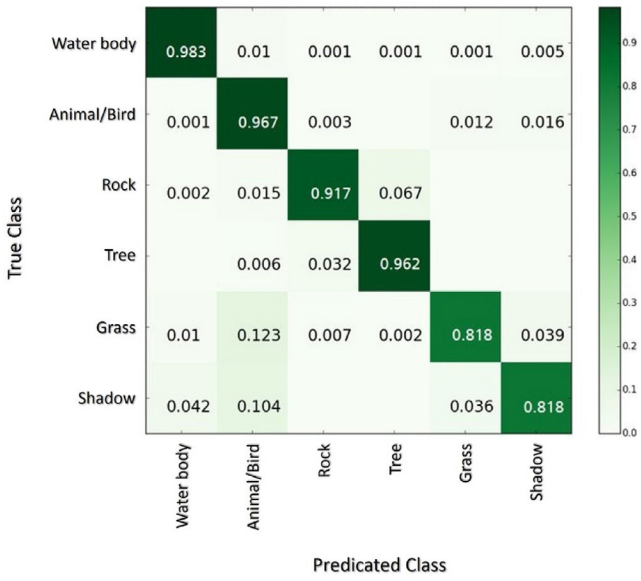

Fig. 17. Normalized confusion matrix.

whereas the minimum accuracy goes to grass and shadow classes at around 0.818. The boundary evaluation over the study area shows that grass and shadows raise complexities as these two classes are shallow and sometimes overlap with water bodies and/or marks. Overall, the classification level evaluation over the study area suggests that the performance of the two-brains optimization framework in relation to change detection and object recognition achieves a high level of accuracy that ranges between 91.3 and 99.6%.

Table 3 shows a summary of classification accuracies of various features inside the Snake gorge using the two-brains optimization framework. The table presents the two parameters of performance and validation indicators, OA and Kappa. The CNN can identify all classes with high degree of accuracy.

To validate the proposed framework further, primarily the DEM, a complexity analysis of its execution time against that of DSM and DTM has been carried out. Fig. 18 depicts the results of the analysis and shows an exponential increase in time as the input size rises. The overall complexity of the proposed framework is lower than that of DSM and DTM and the main reason for that is that the DEM uses raster grids to represent buildings, trees, or other types of vegetation in the fly zone as vertical datum. This yields a smooth DEM which reduces the complexity of detecting water flows.

Table 3
Classification accuracies for various features inside the Snake gorge.

Classified category	Performance and validation indicators	
	Kappa	*OA%*
Water body	0.983	99.6%
Animal/Bird	0.967	98.1%
Rock	0.917	94.9%
Tree	0.962	98%
Grass	0.818	91.3%
Shadow	0.818	91.3%

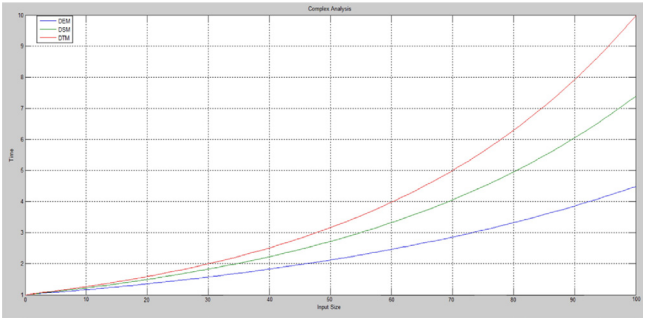

Fig. 18. Complexity analysis of the proposed framework against DSM, and DTM.

5. Conclusion and future direction

Progressively, UAVs are becoming part of the fabric in people's lives. The technology has matured and is considered as an efficient method, perhaps the only one, for delivering various applications and services timely and efficiently. This research has exploited the UAV's primary function of retrieving imagery, over those areas whose morphology poses problems for satellites, to search for water bodies using a combination of a DEM, 3DSCDM and WDM within a deep learning framework. In assessing the feasibility and efficacy of a photogrammetrically derived 3DSCDM with reference to a DEM and a WDM, the combination has retrieved extraordinary invaluable temporal and spatial geomorphic and geologic information whilst searching for water bodies. This work can be useful not only for national and local governments and associations in safe searching for those natural resources that are essential in sustaining human life, but also in supporting safety and security with underground tourist activities.

The research and practical facets of this work have highlighted several challenges addressing of which will open new opportunities:

- Power management on site (battery recharging) without a mandatory return to base when energy levels reduce near the level of safe return,
- Decision making mid-fly (conflict resolution) without human intervention when two or more competing actions yield an impasse.

With regards to on-site power management, approaches being considered include deploying a charging station UAV capable of harvesting renewable energy. With regards to mid-fly decision making, approaches currently being pursued include, among other, serious gaming.

Declaration of competing interests

The authors declare that they have no known competing financial interests or personal relationships that could have appeared to influence the work reported in this paper.

Funding

The authors have contributed equally to this work.

The authors acknowledge the support of Taif University, Saudi Arabia through the research project TURSP-2020/265.

References

[1] S.H. Alsamhi, F. Almalki, O. Ma, M.S. Ansari, B. Lee, Predictive estimation of optimal signal strength from drones over IoT frameworks in smart cities, IEEE Trans. Mob. Comput. (2021) 1, http://dx.doi.org/10.1109/tmc.2021.3074442.

[2] F. Almalki, Utilizing drone for food quality and safety detection using wireless sensors, in: 3rd IEEE International Conference on Information Communication and Signal Processing, ICICSP 2020, 2020, pp. 238–243.

[3] S. Alsamhi, O. Ma, M. Ansari, F. Almalki, Survey on collaborative smart drones and Internet of Things for improving smartness of smart cities, IEEE Access 7 (2019) 128125–128152, http://dx.doi.org/10.1109/ACCESS.2019.2934998.

[4] K. Appeaning Addo, P.-N. Jayson-Quashigah, S.N.A. Codjoe, F. Martey, Drone as a tool for coastal flood monitoring in the Volta Delta, Ghana, Geoenviron. Disasters 5 (1) (2018) http://dx.doi.org/10.1186/s40677-018-0108-2.

[5] M. Govorcin, B. Pribicevic, A. Dapo, Comparison and analysis of software solutions for creation of a digital terrain model using unmanned aerial vehicles, in: 14th International Multidisciplinary Scientific GeoConference SGEM, Albena, Bulgaria, 2014, pp. 17–26.

[6] F.A. Almalki, B.O. Soufiene, S.H. Alsamhi, H. Sakli, A low-cost platform for environmental smart farming monitoring system based on IoT and UAVs, Sustainability 13 (11) (2021) 5908, http://dx.doi.org/10.3390/su13115908.

[7] T. Xiang, G. Xia, L. Zhang, Mini-unmanned aerial vehicle-based remote sensing: Techniques, applications, and prospects, IEEE Geosci. Remote Sens. Mag. 7 (3) (2019) 29–63, http://dx.doi.org/10.1109/MGRS.2019.2918840.

[8] R. Battulwar, M. Zare-Naghadehi, E. Emami, J. Sattarvand, A state-of-the-art review of automated extraction of rock mass discontinuity characteristics using three-dimensional surface models, J. R. Mech. Geotech. Eng. 13 (4) (2021) 920–936, http://dx.doi.org/10.1016/j.jrmge.2021.01.008.

[9] J.T. Ridge, D.W. Johnston, Unoccupied aircraft systems (UAS) for marine ecosystem restoration, Front. Mar. Sci. 7 (2020) http://dx.doi.org/10.3389/fmars.2020.00438.

[10] L. Luo, F. Li, Z. Dai, X. Yang, W. Liu, X. Fang, Terrace extraction based on remote sensing images and digital elevation model in the loess plateau, China, Earth Sci. Inform. 13 (2) (2020) 433–446, http://dx.doi.org/10.1007/s12145-020-00444-x.

[11] B.S. Acharya, et al., Unmanned aerial vehicles in hydrology and water management: Applications, challenges, and perspectives, Water Resour. Res. 57 (11) (2021) http://dx.doi.org/10.1029/2021wr029925.

[12] J.R. Escobar Villanueva, L. Iglesias Martínez, J.I. Pérez Montiel, DEM generation from fixed-wing UAV imaging and LiDAR-derived ground control points for flood estimations, Sensors 19 (14) (2019) 3205, http://dx.doi.org/10.3390/s19143205.

[13] A. Annis, F. Nardi, A. Petroselli, C. Apollonio, E. Arcangeletti, F. Tauro, C. Belli, R. Bianconi, S. Grimaldi, UAV-DEMs for small-scale flood hazard mapping, Water 12 (6) (2020) 1717, http://dx.doi.org/10.3390/w12061717.

[14] M.H. Chaudhry, A. Ahmad, Q. Gulzar, M.S. Farid, H. Shahabi, N. Al-Ansari, Assessment of DSM based on radiometric transformation of UAV data, Sensors 21 (5) (2021) 1649, http://dx.doi.org/10.3390/s21051649.

[15] F. Bandini, T.P. Sunding, J. Linde, O. Smith, I.K. Jensen, C.J. Köppl, M. Butts, P. Bauer-Gottwein, Unmanned aerial system (UAS) observations of water surface elevation in a small stream: Comparison of radar altimetry, LIDAR and photogrammetry techniques, Remote Sens. Environ. 237 (2020) 111487, http://dx.doi.org/10.1016/j.rse.2019.111487.

[16] S. Hemmelder, W. Marra, H. Markies, S.M. De Jong, Monitoring river morphology & bank erosion using UAV imagery – a case study of the river Buëch, Hautes-Alpes, France, Int. J. Appl. Earth Obs. Geoinf. 73 (2018) 428–437, http://dx.doi.org/10.1016/j.jag.2018.07.016.

[17] J.P. Hupy, C.O. Wilson, Modeling streamflow and sediment loads with a photogrammetrically derived UAS digital terrain model: Empirical evaluation from a fluvial aggregate excavation operation, Drones 5 (1) (2021) 20, http://dx.doi.org/10.3390/drones5010020.

[18] J. Haskins, C. Endris, A.S. Thomsen, F. Gerbl, M.C. Fountain, K. Wasson, UAV to inform restoration: A case study from a california tidal marsh, Front. Environ. Sci. 9 (2021) http://dx.doi.org/10.3389/fenvs.2021.642906.

[19] A.A. Gebrehiwot, L. Hashemi-Beni, Three-dimensional inundation mapping using UAV image segmentation and digital surface model, ISPRS Int. J. Geo-Inf. 10 (3) (2021) 144, http://dx.doi.org/10.3390/ijgi10030144.

[20] S.I. Jiménez-Jiménez, W. Ojeda-Bustamante, M. Marcial-Pablo, J. Enciso, Digital terrain models generated with low-cost UAV photogrammetry: Methodology and accuracy, ISPRS Int. J. Geo-Inf. 10 (5) (2021) 285, http://dx.doi.org/10.3390/ijgi10050285.

[21] A. Bernatek-Jakiel, M. Jakiel, Identification of soil piping-related depressions using an airborne LiDAR DEM: Role of land use changes, Geomorphology 378 (2021) 107591, http://dx.doi.org/10.1016/j.geomorph.2020.107591.

[22] Z. Cheng, W. Gong, H. Tang, C.H. Juang, Q. Deng, J. Chen, X. Ye, UAV photogrammetry-based remote sensing and preliminary assessment of the behavior of a landslide in Guizhou, China, Eng. Geol. 289 (2021) 106172, http://dx.doi.org/10.1016/j.enggeo.2021.106172.

[23] J. Cao, W. Leng, K. Liu, L. Liu, Z. He, Y. Zhu, Object-based mangrove species classification using unmanned aerial vehicle hyperspectral images and digital surface models, Remote Sens. 10 (2) (2018) 89, http://dx.doi.org/10.3390/rs10010089.

[24] Y. Shopov Y. Shopov, O. Ognianov, A. Filipov, I.R. Ivanov, Development of technology for remote location of unknown underground cavities and deep-seated rockslides by unmanned air systems (UAS), J. Phys. Conf. Ser. 1368 (2019) 032032, http://dx.doi.org/10.1088/1742-6596/1368/3/032032.

[25] F.A. Almalki, B.O. Soufiene, Modifying Hata-Davidson propagation model for remote sensing in complex environments using a multifactional drone, Sensors 22 (5) (2022) 1786, http://dx.doi.org/10.3390/s22051786.

[26] W. Handayani, Y. Tri Nurteisa, M. Isnaini Sadali, The role of detail spatial data resulted from unmanned aerial vehicle for tourism area planning, in: Sixth Geoinformation Science Symposium, 2019, 11311.

[27] V. González-Jaramillo, A. Fries, J. Bendix, AGB estimation in a tropical mountain forest (TMF) by means of RGB and multispectral images using an unmanned aerial vehicle (UAV), Remote Sens. 11 (12) (2019) 1413, http://dx.doi.org/10.3390/rs11121413.

[28] E. Rødtang, K. Alfredsen, A. Juárez, Drone surveying of volumetric ice growth in a steep river, Front. Remote Sens. 2 (2021) http://dx.doi.org/10.3389/frsen.2021.767073.

[29] A. Minervino Amodio, G. Di Paola, C.M. Rosskopf, Monitoring coastal vulnerability by using DEMs based on UAV spatial data, ISPRS Int. J. Geo-Inf. 11 (3) (2022) 155, http://dx.doi.org/10.3390/ijgi11030155.

[30] S. Alexandris, et al., Integrating drone technology into an innovative agrometeorological methodology for the precise and real-time estimation of crop water requirements, Hydrology 8 (3) (2021) 131, http://dx.doi.org/10.3390/hydrology8030131.

[31] J.-C. Padró, et al., Drone-based identification of erosive processes in open-pit mining restored areas, Land 11 (2) (2022) 212, http://dx.doi.org/10.3390/land11020212.

[32] D.E. Kim, S.-Y. Liong, P. Gourbesville, L. Andres, J. Liu, Simple-yet-effective SRTM DEM improvement scheme for dense urban cities using ANN and remote sensing data: Application to flood modeling, Water 12 (3) (2020) 816, http://dx.doi.org/10.3390/w12030816.

[33] M. Specht, et al., Analysis of methods for determining shallow waterbody depths based on images taken by unmanned aerial vehicles, Sensors 22 (5) (2022) 1844, http://dx.doi.org/10.3390/s22051844.

[34] M. Rusnák, J. Sládek, A. Kidová, M. Lehotský, Template for high-resolution river landscape mapping using UAV technology, Measurement 115 (2018) 139–151, http://dx.doi.org/10.1016/j.measurement.2017.10.023.

[35] T. Berteška, B. Ruzgiene, Photogrammetric mapping based on uav imagery, Geodesy Cartogr. 39 (4) (2013) 158–163, http://dx.doi.org/10.3846/20296991.2013.859781.

[36] M.I. Sameen, B. Pradhan, O.S. Aziz, Classification of very high-resolution aerial photos using spectral-spatial convolutional neural networks, J. Sensors 2018 (2018) 1–12, http://dx.doi.org/10.1155/2018/7195432.

[37] T. Krauz, P. d'Angelo, J. Tian, P. Reinartz, Automatic DEM generation and 3D change detection from satellite imagery, in: European Space Agency Living Planet Symposium, 2013, pp. 1–6.

[38] M. Theile, H. Bayerlein, R. Nai, D. Gesbert, M. Caccamo, UAV coverage path planning under varying power constraints using deep reinforcement learning, in: IEEE/RSJ International Conference on Intelligent Robots and Systems, 2020, pp. 1444–1449, http://dx.doi.org/10.1109/IROS45743.2020.9340934.

[39] X. Li, Z. Yuan, Q. Wang, Unsupervised deep noise modeling for hyperspectral image change detection, Remote Sens. 11 (3) (2019) 258, http://dx.doi.org/10.3390/rs11030258.

[40] G. Muñoz, C. Barrado, E. Çetin, E. Salami, Deep reinforcement learning for drone delivery, Drones 3 (3) (2019) 72, http://dx.doi.org/10.3390/drones3030072.

[41] J. Ou, X. Guo, M. Zhu, W. Lou, Autonomous quadrotor obstacle avoidance based on dueling double deep recurrent Q-learning with monocular vision, Neurocomputing 441 (2021) 300–310, http://dx.doi.org/10.1016/j.neucom.2021.02.017.

[42] F. Escobar, Satellite images of water bodies, kaggle, 2020, https://www.kaggle.com/franciscoescobar/satellite-images-of-water-bodies (Accessed 25 May 2021).